It's Not Easy Being Green: Kinetic Modeling of the Emission Spectrum Observed in STEVE's Picket Fence

L. Claire Gasque[1], Reza Janalizadeh[2], Brian J Harding[1], Justin D Yonker[3], and Deborah Megan Gillies[4]

[1]University of California, Berkeley
[2]Pennsylvania State University
[3]JHU/APL
[4]University of Calgary

September 11, 2023

It's Not Easy Being Green: Kinetic Modeling of the Emission Spectrum Observed in STEVE's Picket Fence

L. Claire Gasque[1], Reza Janalizadeh[2], Brian J. Harding[1], Justin D. Yonker[3], D. Megan Gillies[4]

[1]Space Sciences Laboratory, University of California, Berkeley
[2]Department of Electrical Engineering, The Pennsylvania State University
[3]The Johns Hopkins University Applied Physics Laboratory
[4]Physics and Astronomy Department, University of Calgary

Key Points:

- Local parallel electric fields quantitatively replicate observed picket fence spectra without requiring particle precipitation.
- At 110 km, parallel electric field strengths between 40 and 70 Td (∼80 to 150 mV/m at 110 km) reproduce observed picket fence spectra.
- Quantitative connections between electrodynamics and observable picket fence emissions offer goalposts for future models and experiments.

Corresponding author: L. Claire Gasque, `lcgasque@berkeley.edu`

Abstract

Recent studies suggest that, despite its aurora-like appearance, the picket fence may not be driven by magnetospheric particle precipitation but instead by local electric fields parallel to Earth's magnetic field. Here, we evaluate the parallel electric fields hypothesis by quantitatively comparing picket fence spectra with the emissions generated in a kinetic model driven by parallel electric fields in a realistic neutral atmosphere. We find that sufficiently large parallel electric fields can reproduce the observed ratio of N_2 first positive to oxygen green line emissions, without producing N_2^+ first negative emissions. At a typical picket fence altitude of 110 km, parallel electric fields between 40 and 70 Td (∼80 to 150 mV/m at 110 km) replicate the observations. These findings establish a quantitative connection between electrodynamics and observable picket fence emissions, offering verifiable targets for future models and experiments.

Plain Language Summary

The 'picket fence' is a captivating visual phenomenon featuring vibrant green streaks often seen below the rare purpleish-white arc called STEVE. It occurs in the subauroral sky, closer to the equator than the auroral oval, raising questions about whether it is a type of aurora or a separate phenomenon. Recent hypotheses propose that strong electric fields aligned with Earth's magnetic field might be responsible for creating the picket fence, setting it apart from traditional auroras caused by energetic particles from space colliding with the upper atmosphere. In this study, we compare optical observations of the picket fence to a detailed calculation of the emissions produced by parallel electric fields in the upper atmosphere. The results show that large parallel electric fields can indeed replicate the observed picket fence phenomenon. These findings offer important targets for future picket fence models and experiments. This research demonstrates that the picket fence serves as a valuable testing ground for understanding kinetic chemistry and electrodynamics in Earth's upper atmosphere.

1 Introduction: Debate Over the Picket Fence's Origin

STEVE (Strong Thermal Emission Velocity Enhancement) is a rare ionospheric optical phenomenon characterized by a narrow mauve arc extending thousands of kilometers east/west across the subauroral sky (MacDonald et al., 2018). Below STEVE, vibrant green streaks known as the "picket fence" often appear after the mauve arc develops and occasionally persist after it fades (Yadav et al., 2021; Martinis et al., 2022; Nishimura et al., 2023). STEVEs are associated with strong sub-auroral ion drifts (SAIDs) (Archer, Gallardo-Lacourt, et al., 2019), but the mechanism behind the optical emissions is still debated (Harding et al., 2020).

Early studies proposed that picket fence emissions, like auroras, are generated by magnetospheric particle precipitation (MacDonald et al., 2018; Chu et al., 2019; Nishimura et al., 2019; Bennett & Bourassa, 2021). Like green aurora, the picket fence primarily consists of 557.7 nm green line (GL) emissions (Gillies et al., 2019). However, the picket fence spectrum published by Gillies et al. (2019) and reanalyzed by Mende et al. (2019) lacks 427.8 nm N_2^+ first negative (N_2^+ 1N) emissions, which are ubiquitous and prominent in auroral spectra. The absence cannot be explained by a local N_2 depletion, as Mende et al. (2019) also detect N_2 first positive (N_2 1P) emissions. Instead, Mende et al. (2019) proposed that picket fence emissions result from local electrons energized to between 7.35 eV (sufficient for N_2 1P emissions) and 18.75 eV (sufficient for N_2^+ 1N emissions). They did not describe how electrons might be locally accelerated to such energies.

Recent studies by Lynch et al. (2022) and Mishin and Streltsov (2022) proposed that picket fence emissions arise when electric fields parallel to Earth's magnetic field energize local electrons. Lynch et al. (2022) demonstrate that ionospheric conductance gradients created by SAIDs create large field-aligned currents, potentially triggering tearing-mode instabilities similar to those observed in rayed auroral arcs. Mishin and Streltsov (2022) simulated the ionospheric feedback instability (IFI) under SAID conditions. Their approximate solution of the Boltzmann equation indicated that parallel electric fields generated by the IFI might be sufficient to produce the suprathermal electron population responsible for the picket fence emissions. However, they did not conclusively demonstrate whether this electron population quantitatively reproduces the observed picket fence spectral features.

In this study, we conduct kinetic calculations in a realistic neutral atmosphere from 100 to 180 km, considering all relevant electron-neutral collisions. Additionally, we compare our calculated spectral features with those in ground-based picket fence observations. Our findings demonstrate that local parallel electric fields quantitatively replicate observed picket fence spectra without requiring particle precipitation. Estimating the magnitude of these fields provides a benchmark for future models and observations. This work enables a quantitative comparison between electrodynamic models and observable optical emissions, which previous studies have not achieved.

2 Picket Fence Spectral Observations

The Transition Region Explorer (TREx) Spectrograph in Lucky Lake, Saskatchewan captures visible (385-801 nm) spectral data for a narrow ($\sim$2.1° wide) North/South latitudinal slice of the sky. For additional details about TREx's operation and calibration, refer to Gillies et al. (2019). On April 10, 2018, the same night as the observations presented by Gillies et al. (2019), TREx observed the picket fence several times between 6:28 and 8:00 UT. Figure 1(a) presents a keogram of the observations, showing the total observed luminosity as a function of elevation angle and time. Thin horizontal features brighter than the background are stellar contamination.

Figure 1(b) displays a keogram of the GL portion of the spectrum (555.2-560.7 nm). Picket fence spectra are identified following the method in Gillies et al. (2019) and Mende et al. (2019). We fit a Gaussian function to the GL luminosity with respect to elevation angle at each time step, determining the elevation angle at the peak brightness μ and the standard deviation σ. For luminosity curves with a defined peak at least 200 R above background luminosity, the picket fence spectrum is selected at the elevation bin μ, while background spectra are selected at elevation bins $\pm 3\sigma$ away from μ. Picket fence spectra with stellar contamination are discarded, and contaminated background spectra are replaced by neighboring uncontaminated pixels. Figure 1(c) displays the extracted picket fence spectra (black dots) and the selected poleward (blue triangles pointing up) and equatorward (red triangles pointing down) backgrounds between 6:49 and 7:00 UT.

The picket fence is expected to lie between 97 and 150 km and be approximately aligned with the magnetic field (Archer, St.-Maurice, et al., 2019; Semeter et al., 2020). The black dotted line in Figure 1(d) represents the look direction up the magnetic field, calculated using the International Geomagnetic Reference Field, Version 13 (IGRF13) (Wardinski et al., 2020; Michael, 2021). Our kinetic model described in Section 3 assumes emissions originate from a uniform source at a single altitude, avoiding assumptions about the vertical parallel electric field profile. Consequently, select picket fence spectra closer to the horizon, away from the magnetic field look direction, to reduce the vertical profile intersected by the line-of-sight. Specifically, we use 45 uncontaminated picket fence spectra observed between 6:45 and 7:30 UT, all with elevation angles between 131° and 142°. Figure 1(d) depicts the picket fence observation geometry at 6:52 UT. The observed GL luminosity is projected onto an arc at an arbitrary altitude, and the equatorward and poleward picket fence boundaries are marked by solid red and blue lines, respectively. The observed picket must lie within the wedge formed by these boundaries. Assuming that the picket fences are 5-25 km wide latitudinally (Liang, Zou, et al., 2021), we es-

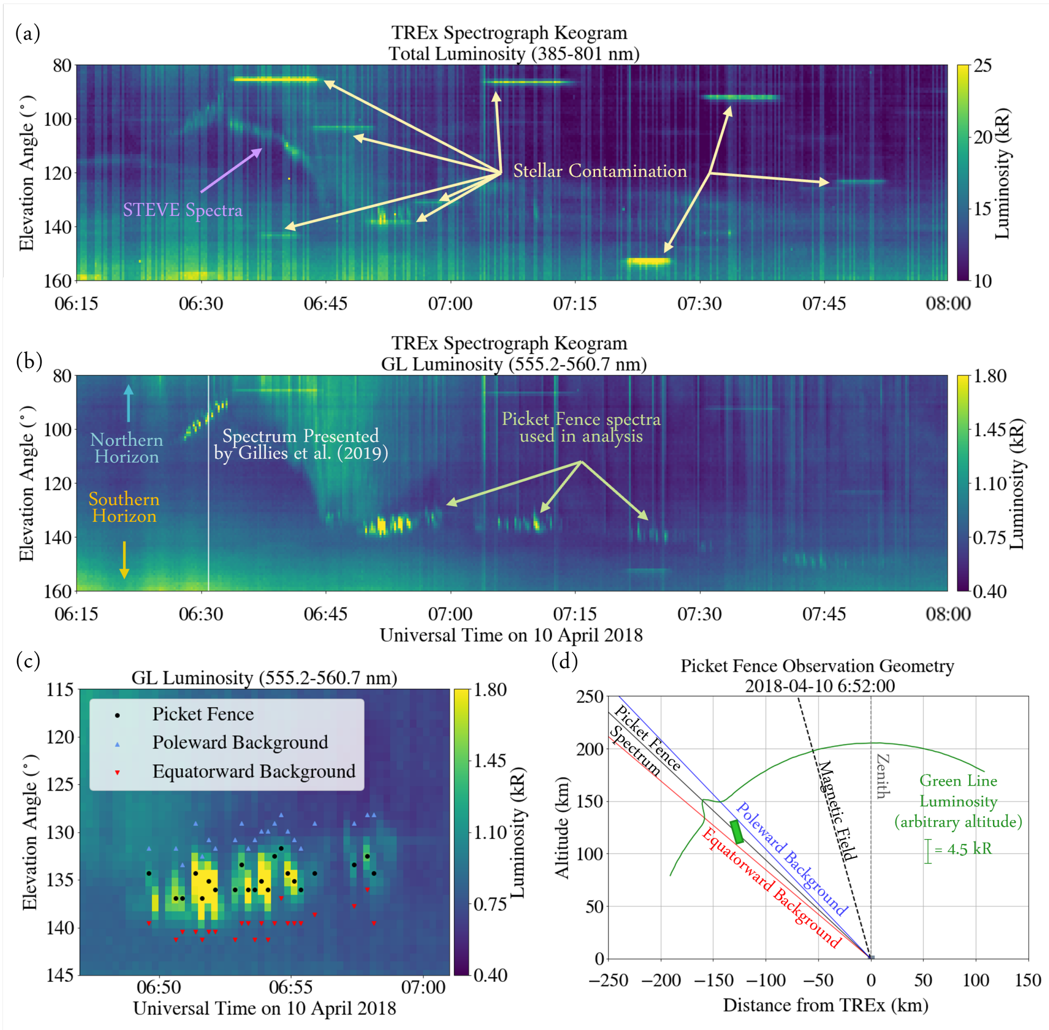

Figure 1. (a) Keogram of total TREx luminosity between 6:15 and 8:00 UT on April 10, 2018, showing STEVE emissions and stellar contamination. (b) Keogram of TREx GL observations (555.2-560.7 nm) during the same period, highlighting the picket fence observations. (c) Picket fence and background spectra extracted between 6:49 and 7:00 UT. Some spectra were removed due to stellar contamination. See text for details of selection process. (d) Approximate observation geometry for picket fence observed at 6:52 UT. The sample picket shown is only a representation as the altitude of the emissions is unknown.

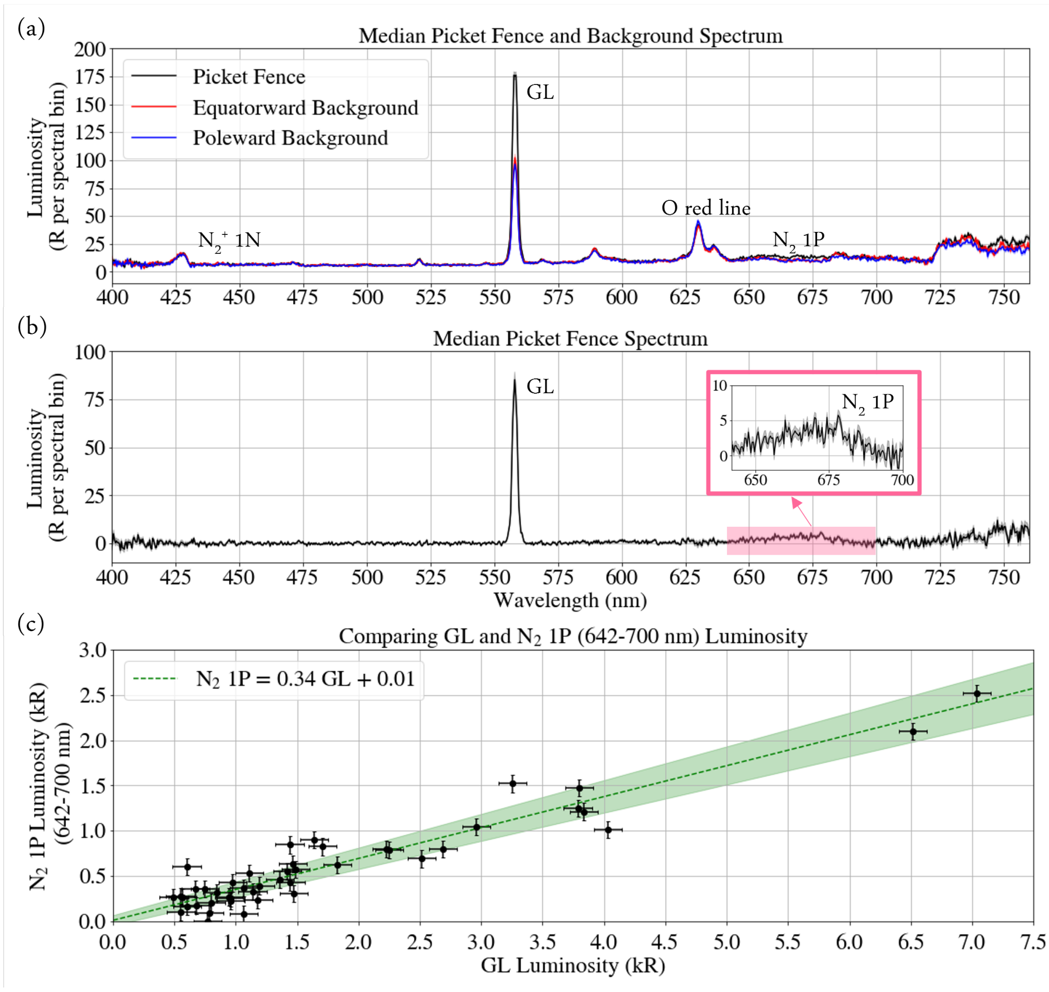

Figure 2. (a) Median picket fence spectrum (black) and poleward (blue) and equatorward (red) background spectra. (b) Median picket fence spectrum after background subtraction. Inset: N_2 1P spectrum (642-700 nm). (c) Ratio of N_2 1P (642-700 nm) to GL luminosity from the TREx observations, scaled to account for atmospheric transmission.

timate that the line-of-sight cuts through no more than 25 km of the altitudinal profile for the selected observations, with most examples cutting through no more than 15 km. Due to these observational constraints, our quantitative results in Section 4 represent vertical averages over a maximum of 25 km.

We isolate individual picket fence spectra by subtracting the average of their poleward and equatorward background spectra. The error in each spectrum is determined by propagating the standard deviation variations in the background spectra at each wavelength through the background subtraction. Figure 2(a) shows the median picket fence and background spectra, while Figure 2(b) displays the median background-subtracted picket fence spectrum. The dominant features are the 557.7 nm GL and the N_2 1P band system, while the 427.8 nm N_2^+ 1N emissions observed in the background spectra are absent in the picket fence spectrum, consistent with the findings of Mende et al. (2019).

Instead of directly comparing the absolute observed brightness to our model results, which requires assuming the picket fence's latitudinal width and the local electron density, we focus on comparing the ratio of N_2 1P and GL luminosities. For the GL, we calculate the luminosity between 555.2-560.7 nm, accounting for the GL's spectral width. For N_2 1P, we calculate the luminosity between 642 and 700 nm. Although N_2 1P emissions extend to infrared (IR) wavelengths and TREx's range extends to 800 nm, we only consider this part of the spectrum to avoid larger errors near the edge of TREx's observational band and complications from O_2 atmospheric absorption above 700 nm.

To quantitatively compare the in situ ratio of N_2 1P to GL emissions, we must consider atmospheric transmission between the emission source and TREx. We apply an atmospheric transmission profile from Figure 1(a) of Morrill et al. (1998), which corresponds to a source at 65 km observed from the ground at an elevation angle of 40°, similar to our observations. While the picket fence occurs at higher altitudes, most atmospheric scattering and absorption occur in the lower atmosphere, so this difference is assumed to be negligible (Meier, 1991). According to Morrill et al. (1998), the transmittance at 557.7 nm for GL is 0.42, and the average transmittance for N_2 1P between 642 and 700 nm is 0.53. This results in a transmittance ratio of $\sim$1.26 between the two features.

We perform linear regression on the data using the model $y = \alpha x + \beta$, where y represents the N_2 1P luminosities, x represents the GL luminosities, α represents the luminosity ratio, and β represents the intercept. Using a Bayesian approach to linear regression with errors in both variables, following the method described by Gull (1989), we estimate the best-fit parameters and their errors. Our analysis yields $\alpha = 0.34 \pm 0.03$ and $\beta = 9.4 \pm 56.9$ R. These results are displayed in Figure 2(c). Mende et al. (2019) conducted a similar analysis without considering transmission effects and found an N_2 1P to GL ratio of 0.39. If we neglect transmission effects, our ratio is $\alpha = 0.43 \pm 0.04$, which is consistent with Mende et al. (2019)'s findings. We note that the ratio for green aurora is 0.72, significantly different from our picket fence results (Vallance Jones, 1974).

3 Kinetic Modeling of Emissions Driven by Parallel Electric Fields

Successful models of mechanisms generating the picket fence must be able to achieve the observed ratio of 0.34 between N_2 1P (642-700 nm) and GL emissions while keeping N_2^+ 1N emissions undetectable. Here, we explore whether a kinetic model driven solely by parallel electric fields can replicate these features. The following subsections outline the modeling process, including determining the atmospheric and ionospheric inputs, analyzing the effect of a parallel electric field on the local electron energy distribution function (EEDF), and employing steady-state kinetic modeling to calculate volume emission rates (VERs) of excited atomic and molecular states. Figure 3 summarizes the modeling process.

3.1 Model Inputs: Atmospheric and Ionospheric Conditions

We use established models to characterize atmospheric, ionospheric, and magnetic field conditions for the time, location, and geomagnetic conditions of the TREx observations described in Section 2. The Naval Research Laboratory's Mass Spectrometer Incoherent Scatter Radar (MSIS) model version 2.1 provided profiles of neutral temperature and densities for eight neutral species (Picone et al., 2002; Emmert et al., 2021, 2022; Lucas, 2023). Ionospheric electron density and temperature profiles were taken from the International Reference Ionosphere 2016 (IRI16) (Bilitza et al., 2017; Ilma, 2017). The magnitude of the magnetic field was obtained from IGRF13 (Wardinski et al., 2020; Michael, 2021). The resulting profiles are shown in Figure S1 of the Supplemental Information.

Using these profiles assumes that picket fence conditions are similar to climatological conditions. However, STEVE and the picket fence are associated with intense SAIDs (MacDonald et al., 2018; Archer, Gallardo-Lacourt, et al., 2019), rare events character-

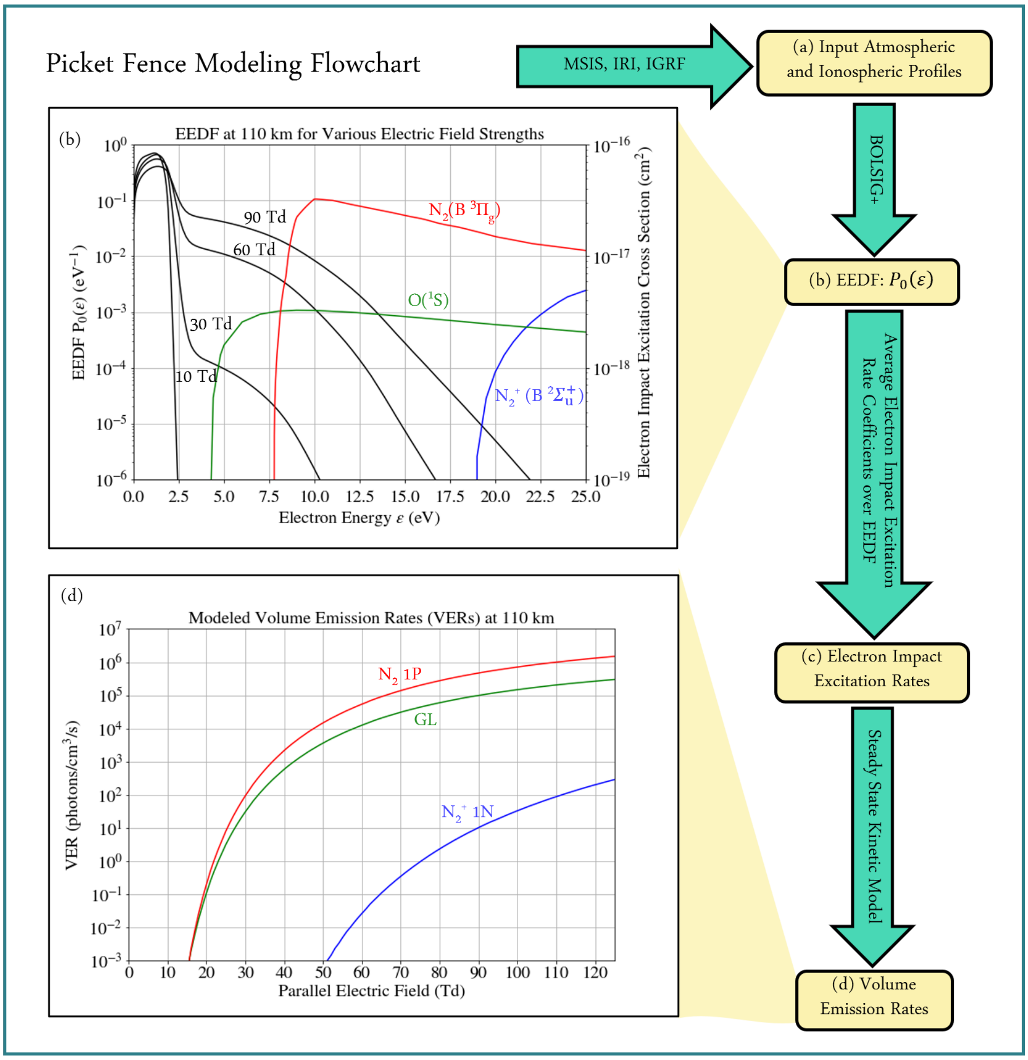

Figure 3. Modeling process flowchart of steps (a) - (d), with subfigures to further elucidate steps (b) and (d). (b) EEDFs at 110 km for different parallel electric field strengths, overlaid with electron impact excitation cross sections for $O(^1S)$, $N_2\,(B^3\Pi_g)$, and $N_2^+\,(B^2\Sigma_u^+)$. (d) VERs at 110 km for GL, N_2 1P, and N_2^+ 1N calculated with the steady state kinetic model.

ized by narrow channels of hot, fast-flowing, and depleted plasma (Liang, St-Maurice, & Donovan, 2021). Although IRI does not replicate these conditions, the ratio between N_2 1P (642-700 nm) and GL emissions is independent of electron density, so this does not affect our results. Additionally, Mishin and Streltsov (2022) suggested that SAID conditions may lead to neutral upwelling, which is not captured by MSIS and which may decrease the O/N_2 ratio at picket fence altitudes. Doubling the O/N_2 ratio input in our model introduces changes on the order of 25% to our electric field magnitude predictions which, while significant, do not alter our qualitative findings.

3.2 Calculating EEDFs and Electron Impact Excitation Rates

We used BOLSIG+ (version 12/2019) (Hagelaar & Pitchford, 2005) to solve the Boltzmann equation, quantifying changes in the EEDF with altitude and parallel electric field strength. BOLSIG+ calculates a steady-state solution under a uniform electric field, so time-dynamics, non-local electron transport, and electric field gradients are not considered. Additionally, we neglect the effect of Coulomb collisions (Gurevich, 1978). Fractional densities of N_2, O_2, and O were obtained from MSIS, while electron impact collisional cross sections of N_2, O_2, and O were obtained from Phelps and Pitchford (1985), Lawton and Phelps (1978), and Laher and Gilmore (1990), respectively.

We consider altitudes between 100 and 180 km, where the 180 km upper bound is well above the expected picket fence altitude (Archer, St.-Maurice, et al., 2019). The 100 km lower bound approximately marks the division between the atmospheric collisional regime, where collisions among excited states are important, and the radiational regime dominated by electron impact excitation (Yonker & Bailey, 2020). We considered reduced parallel electric fields ranging from $E/N = 0$ to 120 Townsend (Td) where E is the electric field in V/m, N is the neutral density in m^{-3}, and 1 Td $= 10^{-21}$ V m^2. The upper limit corresponds to the breakdown field E_k in conventional air at low altitudes (Raizer, 1991, p. 137).

Figure 3(b) displays EEDFs at 110 km for parallel electric fields of 10, 30, 60, and 90 Td (equivalent to 20, 60, 115, and 170 mV/m at 110 km, respectively). The figure highlights several electron impact collisional cross sections: $\mathrm{O}\left(^1S\right)$ in green, $\mathrm{N}_2\left(B^3\Pi_g\right)$ in red, and $\mathrm{N}_2^+\left(B^2\Sigma_u^+\right)$ in blue. Stronger electric fields stretch the tail of the EEDF to higher energies, enhancing high-energy electron populations and increasing electron impact excitation rate coefficients.

3.3 Calculating Volume Emission Rates

To calculate theoretical VERs for N_2 1P, GL, and N_2^+ 1N emissions, we implement a steady-state kinetic model which accounts for additional production and loss processes for excited states of N_2 and O. For N_2 1P emissions, produced through relaxation of the $\mathrm{N}_2\left(B^3\Pi_g\right)$ state to the $\mathrm{N}_2\left(A^3\Sigma_u^+\right)$ state, we account for radiative cascade from higher N_2 triplet states (Meier, 1991). For GL emissions, produced via relaxation of the $\mathrm{O}\left(^1S\right)$ state to the $\mathrm{O}\left(^1D\right)$ state, we incorporate additional $\mathrm{O}\left(^1S\right)$ production via O quenching of $\mathrm{N}_2\left(A^3\Sigma_u^+\right)$. We also consider additional quenching of $\mathrm{O}\left(^1S\right)$ and $\mathrm{N}_2\left(A^3\Sigma_u^+\right)$ by O, O_2, and NO. N_2^+ 1N emissions occur via relaxation of $\mathrm{N}_2^+\left(B^2\Sigma_u^+\right)$ state to the ground state following electron impact ionization (Shemansky & Liu, 2005). For more details about these calculations, see Section S1 of the Supplementary Information.

We compared these calculated VERs to those obtained by inputting our electron impact excitation rates into Yonker and Bailey (2020)'s model, which includes interactions between individual N_2 excited states and resolves the vibrational states of N_2. Between 105 and 150 km, the difference in the N_2 1P to GL emission ratio between our model and Yonker and Bailey (2020)'s is below 15%, demonstrating excellent agreement. At lower altitudes, where the collisional regime dominates, the difference remains below 40%.

Figure 3(d) presents the modeled VERs for N_2 1P, GL, and N_2^+ 1N at 110 km as a function of parallel electric field strength. The VERs are directly proportional to electron density, which may be depleted under SAID conditions, so the actual VERs may be reduced if the picket fence lies within the depleted channel. However, the ratio between these VERs remains independent of the electron density.

4 Comparison with Observations

Figures 4(a) and 4(b) present calculated N_2 1P to GL VER ratios for parallel electric fields in units of Td and mV/m, respectively, where the N_2 1P spectrum has been truncated to only include the 642-700 nm portion. The complete picket fence N_2 1P spectrum has never been measured, so we use an estimated scaling factor of ∼8% determined from modeling of the N_2 1P spectrum in aurora, presented in Table 4.12 of Vallance Jones (1974). The observed ratio and its data-driven uncertainty are indicated in Figures 4(a) and (b) by the black dotted lines and shaded regions, respectively. At 110 km, the observed N_2 1P (642-700 nm) to GL ratio is reproduced for parallel electric field strengths between 40 and 70 Td (∼80 to 150 mV/m at 110 km). Assuming a picket fence width of ∼10 km, a uniform emission source, and electron densities given by IRI, this corresponds to GL luminosities between 0.5 and 31 kR, consistent with observations.

If the N_2 $\left(B^3\Pi_g\right)$ vibrational distribution differs between aurora and the picket fence, the shape of the N_2 1P spectrum may also differ. A test was performed in which our electron impact excitation rates were inputs to Yonker's vibrationally-resolved model; the results suggested the 642-700 nm portion may account for 12-14% of the total N_2 1P spectrum. Adopting this higher scale factor leads to a ∼50% reduction in our predicted parallel electric field strength at 110 km. Obtaining a picket fence N_2 1P spectrum extending into the IR would enhance confidence in our quantitative estimates of parallel electric field strength, although our qualitative findings remain unchanged.

The calculated N_2^+ 1N to GL VER ratios are presented in Figure 4(c). Even for large parallel electric field strengths, this ratio remains below 10^{-3} at picket fence altitudes, undetectable by the TREx spectrograph for even the brightest picket fence events. Thus, we find that parallel electric fields of realistic magnitudes will not produce observable N_2^+ 1N emissions.

These results demonstrate that a model driven by parallel electric fields can reproduce all of the key picket fence spectral features at picket fence altitudes, strongly supporting parallel electric fields as a plausible driving mechanism for picket fence emissions.

5 Discussion and Conclusion

This study provides quantitative evidence that spectral features of picket fence emissions can be reproduced by a kinetic model driven solely by parallel electric fields, offering a substantiated alternative to magnetospheric precipitation, which lacks supporting spectral evidence. As a reference point for future observations and modeling, we find that at 110 km 40-70 Td (∼80-150 mV/m at 110 km) parallel electric fields produce observationally-consistent picket fence spectra. The developed kinetic and chemical modeling tools could be used as post-processors or two-way coupled into global or regional MHD models to simulate the picket fence or its potential connections to other subauroral phenomena such as SAIDs, STEVE, or stable auroral red (SAR) arcs (Gallardo-Lacourt et al., 2021; Harding et al., 2020; Martinis et al., 2022; Gillies et al., 2023; Liang, St-Maurice, & Donovan, 2021).

While we have demonstrated the plausibility of parallel electric fields as a driving mechanism for the picket fence, further measurements are essential to validate or challenge this hypothesis. Our modeling demonstrates that parallel electric fields of mag-

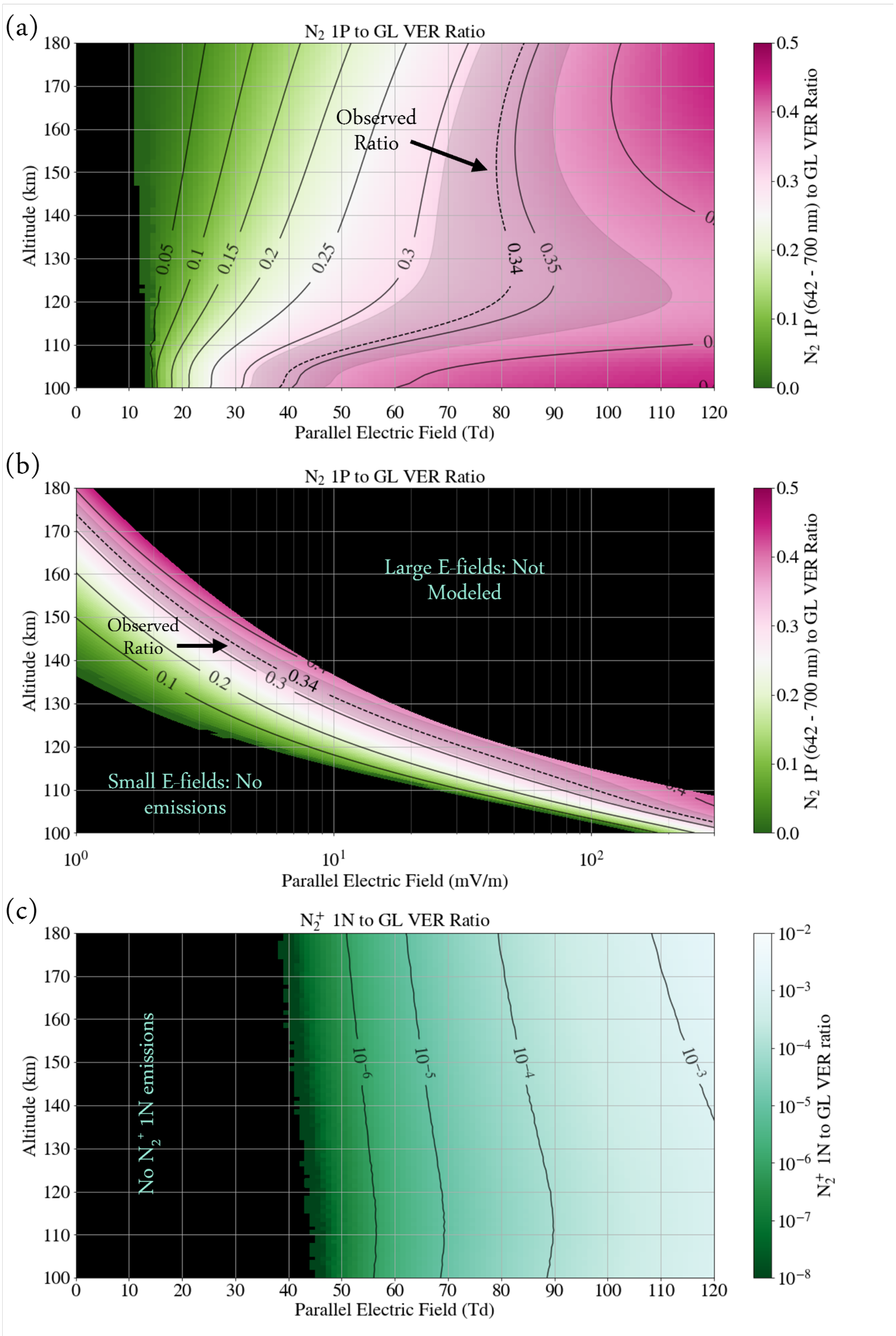

Figure 4. (a) Calculated N_2 1P (642-700 nm) to GL VER ratios. Observed luminosity ratios and margins of error are indicated by the black dotted line and shaded region, respectively. (b) The same as (a), but with parallel electric field strength in mV/m. (c) Calculated N_2^+ 1N (421-431 nm) to GL VER ratios.

nitudes considered here would not generate observable N_2^+ 1N emissions. Therefore, any future observations of N_2^+ 1N emissions in a picket fence would prompt reassessment of this mechanism. Furthermore, Section S2 describes an extension of our model to predict ultraviolet (UV) spectral features of the picket fence, which could be confirmed by space-based observations. For the brightest picket fence events, we find that N_2 Vegard-Kaplan (VK) and Lyman-Birge-Hopfield (LBH) emissions could be promising observational targets. However, N_2 Second Positive (2P) bands and 1356 Å atomic oxygen emissions are unlikely to be observable, as shown in Figure 1S. Additionally, expanding this analysis to include more picket fence spectra would help capture the true extent of the variability in these spectra and further assess the consistency with the parallel electric field driving mechanism.

If parallel electric fields indeed drive picket fence emissions, the structure of the picket fence constrains the electric field's structure. Under the influence of a parallel electric field at picket fence altitudes, the EEDF equilibrates in between ∼0.1 and 50 ms, increasing with altitude (Gurevich, 1978). Given the ∼0.7 s radiative lifetime of $O\left({}^1S\right)$ (Itikawa & Ichimura, 1990), and the several microseconds radiative lifetime of $N_2\left(B^3\Pi_g\right)$ (Eyler & Pipkin, 1983), visible emissions should emerge within 1 s of the parallel electric field onset, depending on the altitude. While electron transport or neutral winds may induce some blurring, the emissions should predominantly trace the parallel electric fields. As a result, the electric fields would exhibit similar structure to the picket fence itself: aligned in a rayed east/west arc, confined between 97 and 150 km in altitude, and organized along the local magnetic field (Archer, St.-Maurice, et al., 2019). However, the non-field-aligned emission 'streaks' below the picket fence (103-108 km) may not trace parallel electric fields, as these are hypothesized to be a consequence of plasma turbulence (Semeter et al., 2020).

While this study refrains from speculating on sources or resulting altitude profiles of parallel electric fields, Lynch et al. (2022) and Mishin and Streltsov (2022) suggest that parallel electric fields could be the consequence of different ionospheric instabilities driven by extreme SAIDs. Lynch et al. (2022) suggest that wave electric fields parallel to the magnetic field, arising from a tearing-mode instability, could drive the picket fence. Although they do not model the magnitude or frequency of these waves, our study's results are applicable to wave electric fields which vary significantly slower than the EEDF equilibration timescale. Mishin and Streltsov (2022)'s simulation of the ionospheric feedback instability yielded maximum field strengths of ∼26 mV/m, occurring at 130-140 km. Our predictions achieved the observed N_2 1P to GL emissions ratio for ∼7 mV/m electric field strengths at 135 km, showing reasonable agreement with Mishin and Streltsov (2022)'s results.

Parallel electric fields may play a significant role in the ionosphere beyond the picket fence. In the auroral region, certain optical features share spectral characteristics with the picket fence and cannot be explained by precipitation. Fragmented aurora-like emissions (FAE) are non-field aligned green patches showing GL and N_2 1P emissions but lacking N_2^+ 1N (Dreyer et al., 2021). Enhanced aurora (EA) consist of thin, bright layers within regular aurora, exhibiting increased N_2 1P relative to N_2^+ 1N (Hallinan et al., 1997). Similar to the picket fence, both FAE and EA are suggested to result from suprathermal electron populations locally generated by parallel electric fields or wave-particle interactions (Hallinan et al., 1997; Dreyer et al., 2021). Karlsson et al. (2005) simulated EA using a simple auroral current model, generating parallel electric fields with maximum strength of ∼30 mV/m peaking between 80-120 km. Collectively, this suggests that the picket fence might represent one example of a class of aurora-like emissions generated locally by parallel electric fields, not particle precipitation, although the sources of these fields may differ. These findings underscore the potential significance of parallel electric fields. In particular, since visible and ultraviolet auroral observations are increasingly used to trace particle precipitation and infer magnetospheric activity, it is important to better understand and quantify other sources of emission beyond particle precipitation. Thus, investigating the prevalence and sources of these parallel electric fields warrants further attention from the broader scientific community.

The most definitive way to verify the existence of these parallel electric fields is with in situ measurements. While magnetospheric parallel electric fields have long been associated with auroral particle acceleration and precipitation (Marklund, 1993; Shelley, 1995; Paschmann et al., 2003), static current closure models predict parallel electric fields from the ionospheric F-region to the E-region to be orders of magnitude weaker than perpendicular fields (μV/m rather than mV/m) (e.g. Farley Jr, 1959). Ionospheric electric field measurements routinely assume zero parallel electric field when deriving a full vector perpendicular field from two-dimensional measurements (Pfaff et al., 2021). However, satellite measurements of enhanced downward currents and modeling of the ionospheric response suggest significant parallel fields in the collisional base of the D and E regions (Marklund et al., 1997; Karlsson & Marklund, 1998), but to our knowledge, no measurements have probed the existence of these fields. Confirming the existence of these fields is crucial for advancing our understanding of a wide variety of phenomena in the auroral and subauroral regions. Based on our study's results, we propose that attempting to measure these electric fields in situ should be a priority for the space physics community.

Acknowledgments

We express our gratitude to Stephen Mende and John Bonnell for their inspiration and valuable input in this study. We also acknowledge the University of Colorado Space Weather Technology, Research and Education Center for providing pyMSIS. Partial support for this work was provided by NSF grant AGS-2010088 to Pennsylvania State University, NASA grant 80NSSC21K1386 to the University of California, Berkeley, and the Robert P. Lin Fellowship.

Data Availability Statement

The TREx data used in this study is available freely from https://data.phys.ucalgary.ca/.

References

Archer, W., Gallardo-Lacourt, B., Perry, G. W., St.-Maurice, J.-P., Buchert, S. C., & Donovan, E. (2019). Steve: The optical signature of intense subauroral ion drifts. *Geophys. Res. Lett.*, *46*(12), 6279–6286.

Archer, W., St.-Maurice, J.-P., Gallardo-Lacourt, B., Perry, G., Cully, C., Donovan, E., … Eurich, D. (2019). The vertical distribution of the optical emissions of a Steve and Picket Fence event. *Geophys. Res. Lett.*, *46*(19), 10719–10725.

Bennett, C. L., & Bourassa, N. (2021). Improved analysis of STEVE photographs. *J. Geophys. Res.: Space Phys.*, *126*(4), e2020JA027843.

Bilitza, D., Altadill, D., Truhlik, V., Shubin, V., Galkin, I., Reinisch, B., & Huang, X. (2017). International reference ionosphere 2016: From ionospheric climate to real-time weather predictions. *Space Weather*, *15*(2), 418–429.

Chu, X., Malaspina, D., Gallardo-Lacourt, B., Liang, J., Andersson, L., Ma, Q., … others (2019). Identifying STEVE's magnetospheric driver using conjugate observations in the magnetosphere and on the ground. *Geophys. Res. Lett.*, *46*(22), 12665–12674.

Dreyer, J., Partamies, N., Whiter, D., Ellingsen, P. G., Baddeley, L., & Buchert, S. C. (2021). Characteristics of fragmented aurora-like emissions (FAEs) observed on Svalbard. In *Annales Geophysicae* (Vol. 39, pp. 277–288).

Emmert, J. T., Drob, D. P., Picone, J. M., Siskind, D. E., Jones Jr, M., Mlynczak, M., … others (2021). NRLMSIS 2.0: A whole-atmosphere empirical model of temperature and neutral species densities. *Earth Space Sci.*, *8*(3), e2020EA001321.

Emmert, J. T., Jones Jr, M., Siskind, D. E., Drob, D. P., Picone, J. M., Stevens, M., ... others (2022). NRLMSIS 2.1: An empirical model of nitric oxide incorporated into MSIS. *J. Geophys. Res.: Space Phys.*, *127*(10), e2022JA030896.

Eyler, E., & Pipkin, F. (1983). Lifetime measurements of the $B^3\Pi_g$ state of N_2 using laser excitation. *J. Chem. Phys.*, *79*(8), 3654–3659.

Farley Jr, D. (1959). A theory of electrostatic fields in a horizontally stratified ionosphere subject to a vertical magnetic field. *J. Geophys. Res.*, *64*(9), 1225–1233.

Gallardo-Lacourt, B., Frey, H., & Martinis, C. (2021). Proton aurora and optical emissions in the subauroral region. *Space Sci. Rev.*, *217*, 1–36.

Gillies, D. M., Donovan, E., Hampton, D., Liang, J., Connors, M., Nishimura, Y., ... Spanswick, E. (2019). First observations from the TREx spectrograph: The optical spectrum of STEVE and the picket fence phenomena. *Geophys. Res. Lett.*, *46*(13), 7207–7213.

Gillies, D. M., Liang, J., Gallardo-Lacourt, B., & Donovan, E. (2023). New insight into the transition from a SAR arc to STEVE. *Geophys. Res. Lett.*, *50*(6), e2022GL101205.

Gull, S. F. (1989). Bayesian data analysis: Straight-line fitting. In *Maximum Entropy and Bayesian Methods: Cambridge, England, 1988* (pp. 511–518). Springer.

Gurevich, A. V. (1978). *Nonlinear Phenomena in the Ionosphere.* New York, NY: Springer-Verlag.

Hagelaar, G., & Pitchford, L. C. (2005). Solving the Boltzmann equation to obtain electron transport coefficients and rate coefficients for fluid models. *Plasma Sources Sci. Technol.*, *14*(4), 722.

Hallinan, T., Kimball, J., Stenbaek-Nielsen, H., & Deehr, C. (1997). Spectroscopic evidence for suprathermal electrons in enhanced auroras. *J. Geophys. Res.: Space Phys.*, *102*(A4), 7501–7508.

Harding, B. J., Mende, S. B., Triplett, C. C., & Wu, Y.-J. J. (2020). A mechanism for the STEVE continuum emission. *Geophys. Res. Lett.*, *47*(7), e2020GL087102.

Ilma, R. (2017, Jan). rilma/pyiri2016: Official release of the iri2016 wrapper in python.
doi: 10.5281/zenodo.240895

Itikawa, Y., & Ichimura, A. (1990). Cross sections for collisions of electrons and photons with atomic oxygen. *J. Phys. Chem. Ref. Data*, *19*(3), 637–651.

Karlsson, T., & Marklund, G. (1998). Simulations of effects of small-scale auroral current closure in the return current region. *Physics of Space Plasmas*, *15*, 401.

Karlsson, T., Marklund, G., Brenning, N., & Axnäs, I. (2005). On enhanced aurora and low-altitude parallel electric fields. *Physica Scripta*, *72*(5), 419.

Laher, R. R., & Gilmore, F. R. (1990). Updated excitation and ionization cross sections for electron impact on atomic oxygen. *J. Phys. Chem. Ref. Data*, *19*(1), 277–305.

Lawton, S., & Phelps, A. (1978). Excitation of the $b^1\Sigma_g^+$ state of O_2 by low energy electrons. *J. Chem. Phys.*, *69*(3), 1055–1068.

Liang, J., St-Maurice, J., & Donovan, E. (2021). A time-dependent two-dimensional model simulation of lower ionospheric variations under intense SAID. *J. Geophys. Res.: Space Phys.*, *126*(12), e2021JA029756.

Liang, J., Zou, Y., Nishimura, Y., Donovan, E., Spanswick, E., & Conde, M. (2021). Neutral wind dynamics preceding the STEVE occurrence and their possible preconditioning role in STEVE formation. *J. Geophys. Res.: Space Phys.*, *126*(3), e2020JA028505.

Lucas, G. (2023, Jan). pymsis. doi: 10.5281/zenodo.7581692

Lynch, K. A., McManus, E., Gutow, J., Burleigh, M., & Zettergren, M. (2022). An ionospheric conductance gradient driver for subauroral picket fence visible signatures near STEVE events. *J. Geophys. Res.: Space Phys.*, *127*(12), e2022JA030863.

MacDonald, E. A., Donovan, E., Nishimura, Y., Case, N. A., Gillies, D. M., Gallardo-Lacourt, B., … others (2018). New science in plain sight: Citizen scientists lead to the discovery of optical structure in the upper atmosphere. *Sci. Adv.*, *4*(3), eaaq0030.

Marklund, G. (1993). Viking investigations of auroral electrodynamical processes. *J. Geophys. Res.: Space Phys.*, *98*(A2), 1691–1704.

Marklund, G., Karlsson, T., & Clemmons, J. (1997). On low-altitude particle acceleration and intense electric fields and their relationship to black aurora. *J. Geophys. Res.: Space Phys.*, *102*(A8), 17509–17522.

Martinis, C., Griffin, I., Gallardo-Lacourt, B., Wroten, J., Nishimura, Y., Baumgardner, J., & Knudsen, D. (2022). Rainbow of the night: First direct observation of a SAR arc evolving into STEVE. *Geophys. Res. Lett.*, *49*(11), e2022GL098511.

Meier, R. (1991). Ultraviolet spectroscopy and remote sensing of the upper atmosphere. *Space Sci. Rev.*, *58*(1), 1–185.

Mende, S., Harding, B., & Turner, C. (2019). Subauroral green steve arcs: Evidence for low-energy excitation. *Geophys. Res. Lett.*, *46*(24), 14256–14262.

Michael. (2021, Oct). space-physics/igrf: Robust build, matlab unit test. doi: 10.5281/zenodo.5560949

Mishin, E., & Streltsov, A. (2022). On the kinetic theory of subauroral arcs. *J. Geophys. Res.: Space Phys.*, *127*(8), e2022JA030667.

Morrill, J., Bucsela, E., Pasko, V., Berg, S., Heavner, M., Moudry, D., … Sentman, D. (1998). Time resolved N_2 triplet state vibrational populations and emissions associated with red sprites. *J. Atmos. Sol. Terr. Phys.*, *60*(7-9), 811–829.

Nishimura, Y., Dyer, A., Kangas, L., Donovan, E., & Angelopoulos, V. (2023). Unsolved problems in strong thermal emission velocity enhancement (STEVE) and picket fence. *Front. Astron. Space Sci.*, *10*, 3.

Nishimura, Y., Gallardo-Lacourt, B., Zou, Y., Mishin, E., Knudsen, D., Donovan, E., … Raybell, R. (2019). Magnetospheric signatures of STEVE: Implications for the magnetospheric energy source and interhemispheric conjugacy. *Geophys. Res. Lett.*, *46*(11), 5637–5644.

Paschmann, G., Haaland, S., Treumann, R., & Treumann, R. A. (2003). *Auroral plasma physics* (Vol. 15). Springer Science & Business Media.

Pfaff, R., Uribe, P., Fourre, R., Kujawski, J., Maynard, N., Acuna, M., … others (2021). The vector electric field investigation (VEFI) on the C/NOFS satellite. *Space Sci. Rev.*, *217*, 1–88.

Phelps, A., & Pitchford, L. (1985). Anisotropic scattering of electrons by N_2 and its effect on electron transport. *Phys. Rev. A*, *31*(5), 2932.

Picone, J., Hedin, A., Drob, D. P., & Aikin, A. (2002). NRLMSISE-00 empirical model of the atmosphere: Statistical comparisons and scientific issues. *J. Geophys. Res.: Space Phys.*, *107*(A12), SIA–15.

Raizer, Y. P. (1991). *Gas Discharge Physics.* New York, NY: Springer-Verlag.

Semeter, J., Hunnekuhl, M., MacDonald, E., Hirsch, M., Zeller, N., Chernenkoff, A., & Wang, J. (2020). The mysterious green streaks below STEVE. *AGU Advances*, *1*(4), e2020AV000183.

Shelley, E. (1995). The auroral acceleration region: The world of beams, conies, cavitons, and other plasma exotica. *Rev. Geophys.*, *33*(S1), 709–714.

Shemansky, D. E., & Liu, X. (2005). Evaluation of electron impact excitation of $N_2 X^1\Sigma_g^+(0)$ into the N_2^+ $X^2\Sigma_g^+(v)$, $A^2\Pi_u(v)$, and $B^2\Sigma_u^+(v)$ states. *J. Geophys. Res.: Space Phys.*, *110*(A7).
Vallance Jones, A. (1974). *Aurora.* D. Reidel publishing company.
Wardinski, I., Saturnino, D., Amit, H., Chambodut, A., Langlais, B., Mandea, M., & Thebault, E. (2020). Geomagnetic core field models and secular variation forecasts for the 13th International Geomagnetic Reference Field (IGRF-13). *Earth, Planets and Space*, *72*(1), 1–22.
Yadav, S., Shiokawa, K., Otsuka, Y., Connors, M., & St Maurice, J.-P. (2021). Multi-wavelength imaging observations of STEVE at Athabasca, Canada. *J. Geophys. Res.: Space Phys.*, *126*(2), 2020JA028622.
Yonker, J. D., & Bailey, S. M. (2020). $N_2(A)$ in the terrestrial thermosphere. *J. Geophys. Res.: Space Phys.*, *125*(1), e2019JA026508.

JOURNAL OF GEOPHYSICAL RESEARCH

Supporting Information for "It's Not Easy Being Green: Kinetic Modeling of the Emission Spectrum Observed in STEVE's Picket Fence"

L. Claire Gasque[1], Reza Janalizadeh[2], Brian J. Harding[1], Justin D. Yonker[3],

D. Megan Gillies[4]

[1]University of California, Berkeley, Space Sciences Laboratory

[2]The Pennsylvania State University, Department of Electrical Engineering

[3]The Johns Hopkins University Applied Physics Laboratory

[4]University of Calgary, Physics and Astronomy Department

Contents of this file

Introduction

The supporting information below contains details of the kinetic modeling used to determine volume emission rates (VERs) for various spectral features under the influence of electric fields parallel to the magnetic field in a realistic atmosphere.

Text S1 describes the detailed modeling needed for the main results of the paper: determining whether, using a kinetic model driven only by parallel electric fields, it is possible to obtain the observed ratio of N_2 1st positive (N_2 1P) to Oxygen 557.7 nm green line (GL) emissions while simultaneously not producing N_2^+ first negative (N_2^+ 1N) emissions. Tables S1 and S2 give the rates used for the quenching reactions and radiative cascade, respectively. Figure S1 presents the atmospheric and ionospheric density profiles used in the modeling.

Text S2 describes an extension of this modeling to predict whether, under this mechanism, emission features in the ultra-violet (UV) spectral range might be observable in space-based observations of the picket fence. The detailed results of this analysis are shown in Figure S2.

Text S1. Detailed Steady State Kinetic Calculations of N_2 1P and GL VERs

Atmospheric and ionospheric density profiles used in the modeling described in this section are shown in Figure S1.

N_2 1P emissions are produced through the rapid relaxation of the $N_2\,(B^3\Pi_g)$ state to the $N_2\,(A^3\Sigma_u^+)$ state. Atmospheric quenching effects are negligible. Radiative cascade from higher energy states, including $N_2\,(W^3\Delta_u)$, $N_2\,(B'\,^3\Sigma_u^-)$, and $N_2\,(C^3\Pi_u)$, significantly contribute to the total $N_2\,(B^3\Pi_g)$ population (Vallance Jones, 1974). Only half of the population excited by electron impact in the $N_2\,(C^3\Pi_u)$ state contributes to the cascade due to a pre-dissociation branching ratio of 0.5 (Porter et al., 1976). Contributions from the

$N_2\left(E^3\Sigma_g^+\right)$ and $N_2\left(D^3\Sigma_u^+\right)$ states, which have small excitation cross sections, are omitted, following Meier (1991). Considering that we do not resolve individual vibrational levels of N_2, contributions from reverse first positive transitions, which comprise the relaxation of higher vibrational levels of $N_2\left(A^3\Sigma_u^+\right)$ to lower vibrational levels of $N_2\left(B^3\Pi_g\right)$, are also omitted. The N_2 1P VER is obtained by summing the direct electron impact excitation rate and the rate of radiative cascade to the $N_2\left(B^3\Pi_g\right)$ state. Balancing production and loss under the steady-state assumption allows us to calculate the total N_2 1P VER. This balance can be described by the equation:

$$n_e n_{N_2}\left(k_{e,N_2(B^3\Pi_g)} + k_{e,N_2\left(B'\,^3\Sigma_u^-\right)} + k_{e,N_2(W^3\Delta_u)} + 0.5k_{e,N_2(C^3\Pi_u)}\right) = n_{N_2(B^3\Pi_g)}k_{N_2\ 1P} \quad (1)$$

where n_X refers to the density of species or state X in cm^{-3}, $k_{e,Y}$ is the electron impact excitation of excited state Y from the ground state in cm^3/s (obtained from BOLSIG+), and $k_{N_2\ 1P}$ is the radiative transition frequency for the N_2 1P transition in units of 1/s (see Table S2). The term on the right hand side represents the N_2 1P volume emission rate in units of photons/cm^3/s.

GL emissions occur via relaxation of the $\mathrm{O}(^1S)$ state to the $\mathrm{O}(^1D)$ state. The $\mathrm{O}(^1S)$ state can be excited by electron impact and by O quenching of $N_2\left(A^3\Sigma_u^+\right)$. $N_2\left(A^3\Sigma_u^+\right)$ is formed through electron impact excitation and radiative cascade from the $N_2\left(B^3\Pi_g\right)$ state. The $N_2\left(A^3\Sigma_u^+\right)$ state undergoes radiative decay to the N_2 ground state and is additionally quenched through collisions with O and O_2 (Campbell et al., 2006). This process is described by the equation:

$$n_e n_{N_2} k_{e,N_2\left(A^3\Sigma_u^+\right)} + n_{N_2(B^3\Pi_g)} k_{N_2\ 1P} = \\ n_{N_2\left(A^3\Sigma_u^+\right)} \left(k_{VK} + n_O \left(k_{Q1} + k_{Q2} + k_{Q3}\right) + n_{NO} k_{Q4} + n_{O_2} k_{Q5}\right) \tag{2}$$

where k_{Qx} represents the rate coefficient for quenching reaction x in cm^3/s. These quenching reactions and their rates are listed in Table S1. k_{VK} is the radiative transition rate for the Vegard-Kaplan bands, given in Table S2. From the above equation, we can calculate the $N_2\,(A^3\Sigma_u^+)$ state density and determine the contribution to the $O(^1S)$ state from the quenching reaction.

Quenching of the $O(^1S)$ state is mainly caused by collisions with O_2, while quenching from other species has a minimal effect (less than 10%) at picket fence altitudes. However, we also include quenching by O and NO. The balance for $O(^1S)$ is expressed as:

$$n_e n_O k_{e,O(^1S)} + n_{N_2\left(A^3\Sigma_u^+\right)} n_O k_{Q1} = \\ n_{O(^1S)} \left(k_{557.7\text{ nm}} + n_O k_{Q6} + n_{O_2} \left(k_{Q7} + k_{Q8}\right) + n_{NO} \left(k_{Q9} + k_{Q10}\right)\right) \tag{3}$$

where, again, the quenching reaction rates are given in Table S1 and the radiative transition rate $k_{557.7\text{ nm}}$ is given in Table S1. The total GL VER is obtained by solving the above equation for $n_{O(^1S)} k_{557.7\text{ nm}}$.

N_2^+ 1N emissions occur through electron impact ionization of N_2, followed by rapid relaxation of the resulting N_2^+ ion in the excited $N_2^+\,(B^2\Sigma_u^+)$ state to the ground state. Quenching is negligible at picket fence altitudes. Therefore, the electron impact excitation is the sole contributor to the N_2^+ 1N VER. We obtained electron impact excitation collisional cross sections for the $N_2^+\,(B^2\Sigma_u^+)$ state from Shemansky and Liu (2005).

Text S2. Calculating VERs for Various UV Emissions

We can extend our model to predict ultraviolet (UV) picket fence spectral features which may make good targets for future space-based observations. To do so, we calculate

VERs for the N_2 Vegard-Kaplan (VK), Lyman-Birge-Hopfield (LBH), and Second Positive (2P) bands, as well as the 1356 $\AA$ atomic oxygen emission (Meier, 1991; Liu & Pasko, 2005; Eastes, 2000). The dominant source of each of these emissions is direct electronic excitation which is calculated from BOLSIG+, as described in Section 3.2, as well as some cascade contributions from higher energy states, described below. We do not estimate the 1304 $\AA$ atomic oxygen emission due to complications arising from multiple scattering, which is beyond the scope of this study. Emissions from N and NO are not considered in this analysis.

The N_2 VK bands are generated by the relaxation of the $N_2\,(A^3\Sigma_u^+)$ state to the ground state, and the VK VER is obtained as part of our GL VER calculation (Equation 2). The N_2 2P emissions result from the relaxation of the $N_2\,(C^3\Pi_u)$ state to the $N_2\,(B^3\Pi_g)$ state, which we determined while examining the radiative cascade contribution to the N_2 1P VER (Equation 1).

The N_2 LBH bands (120-280 nm) form when the excited $N_2\,(a^1\Pi_g)$ state relaxes to the ground state. Since the quenching altitude for $N_2\,(a^1\Pi_g)$ is around 77 km, it is not significantly quenched at picket fence altitudes (Liu & Pasko, 2005). We do not consider the radiative and collisional cascades from $N_2\,(a'\,{}^1\Sigma_u)$ and $N_2\,(w^1\Delta_u)$, which could increase the LBH band system emissions by a factor of approximately 1.6 (Eastes, 2000).

The 1356 Å atomic oxygen emission occurs when the $O(3s^5S)$ state relaxes to its ground state. We also consider the cascade contribution from the higher $O(3p^5P)$ state, but disregard cascade from other higher quintet states. We also neglect the effects of multiple scattering and absorption from O_2, both of which can significantly reduce the total observable emissions depending on the observation geometry (Meier, 1991).

The full results of this modeling are shown in Figure S2. At 110 km and 55 Td, we find the N_2 VK, N_2 LBH, N_2 2P, and O 1356 Å to GL ratios to be 0.28, 0.24, 0.15, and 0.006, respectively. For the brightest event that we observed, which is about 7 kR in the GL after accounting for atmospheric transmission, we expect that only N_2 VK and LBH bands would emit enough to be observed while N_2 2P and O 1356 Å are likely not good targets for future observations. Any observational comparisons will additionally need to account for viewing angle, absorption, multiple scattering, and instrumental effects.

Figure S1

Figure S2

Table S1

Table S2

References

Campbell, L., Cartwright, D. C., Brunger, M. J., & Teubner, P. J. O. (2006). Role of electronic excited n2 in vibrational excitation of the n2 ground state at high latitudes. *J. Geophys. Res.: Space Phys.*, *111*(A9).

Eastes, R. W. (2000). Modeling the n2 lyman-birge-hopfield bands in the dayglow: Including radiative and collisional cascading between the singlet states. *J. Geophys. Res.: Space Phys.*, *105*(A8), 18557–18573.

Eyler, E., & Pipkin, F. (1983). Lifetime measurements of the $B^3\Pi_g$ state of N_2 using laser excitation. *J. Chem. Phys.*, *79*(8), 3654–3659.

Grubbs, G., Michell, R., Samara, M., Hampton, D., Hecht, J., Solomon, S., & Jahn, J.-M. (2018). A comparative study of spectral auroral intensity predictions from multiple electron transport models. *J. Geophys. Res.: Space Phys.*, *123*(1), 993–1005.

Liu, N., & Pasko, V. P. (2005). Molecular nitrogen LBH band system far-UV emissions of sprite streamers. *Geophysical Research Letters*, *32*(5).

Meier, R. (1991). Ultraviolet spectroscopy and remote sensing of the upper atmosphere. *Space Sci. Rev.*, *58*(1), 1–185.

Porter, H. S., Jackman, C. H., & Green, A. E. S. (1976). Efficiencies for production of atomic nitrogen and oxygen by relativistic proton impact in air. *Journal of Chemical Physics*, *65*, 154-167.

Shemansky, D. E., & Liu, X. (2005). Evaluation of electron impact excitation of $\mathrm{N}_2 X^1\Sigma_g^+(0)$ into the N_2^+ $X^2\Sigma_g^+(v)$, $A^2\Pi_u(v)$, and $B^2\Sigma_u^+(v)$ states. *J. Geophys. Res.: Space Phys.*, *110*(A7).

Strickland, D., Bishop, J., Evans, J., Majeed, T., Shen, P., Cox, R., ... Huffman, R. (1999). Atmospheric ultraviolet radiance integrated code (auric): Theory, software architecture, inputs, and selected results. *Journal of Quantitative Spectroscopy and Radiative Transfer*, *62*(6), 689–742.

Vallance Jones, A. (1974). *Aurora.* D. Reidel publishing company.

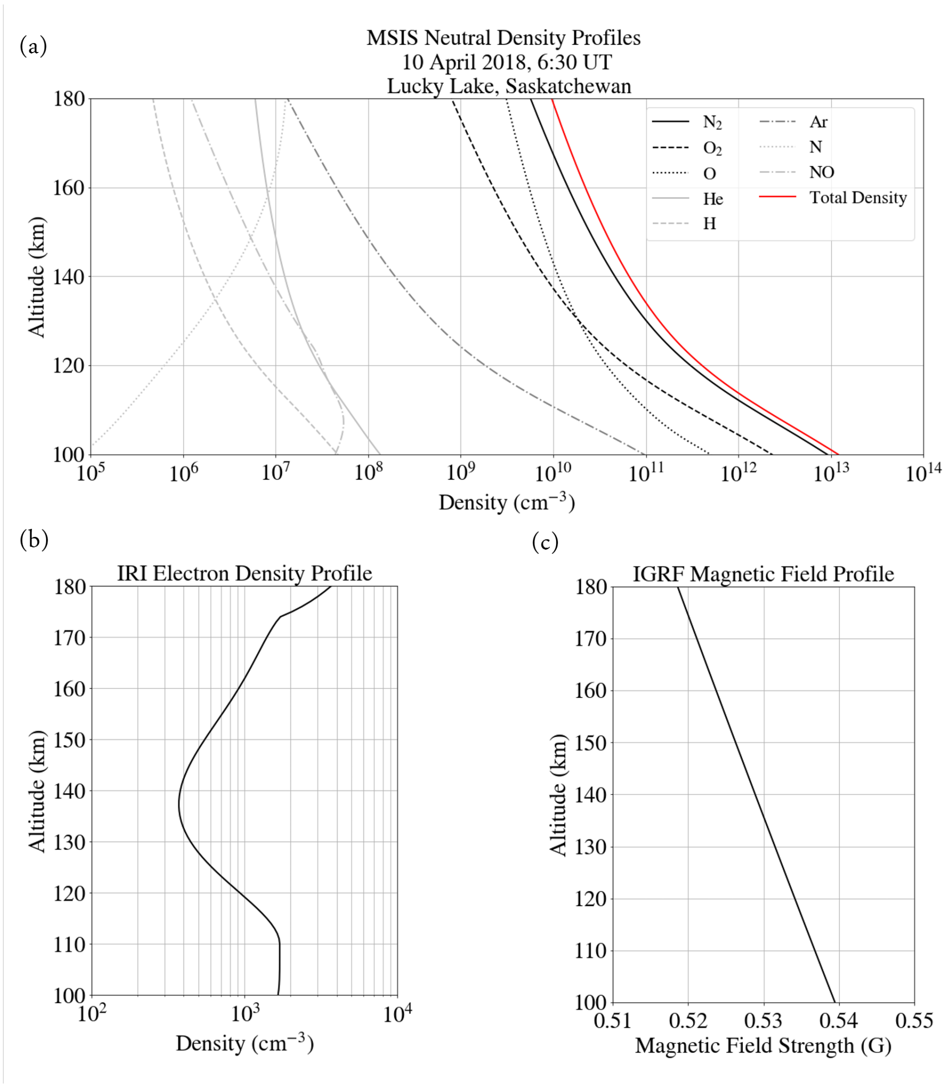

Figure S1. Modeled atmospheric and ionospheric profiles from the time and location of the TREx observations. (a) Neutral atmospheric density profiles from MSIS. (b) Electron density profile from IRI. (c) Magnetic field strength profile obtained from IGRF.

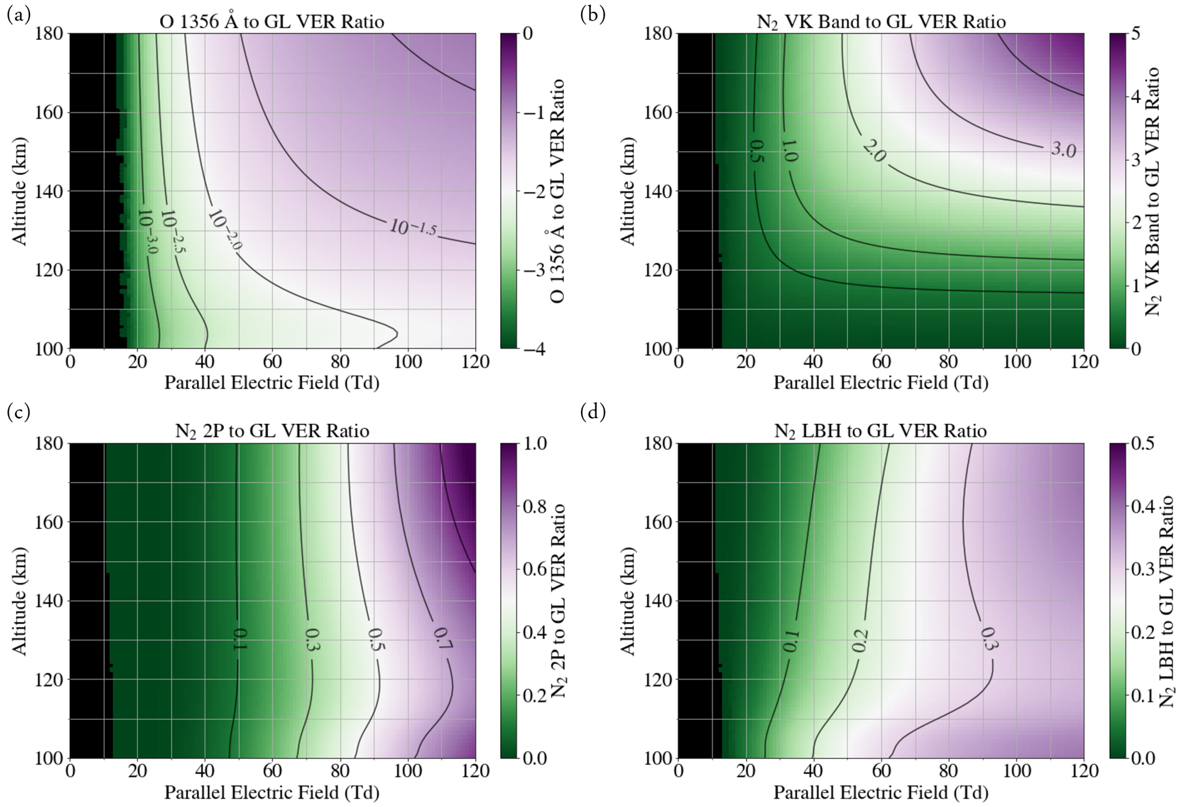

Figure S2. Calculated VER Ratios of various UV emissions to GL as a function of altitude and parallel electric field strength. (a) O 1356 Å (b) VK Bands (c) N_2 2P (d) N_2 LBH.

Reaction #	Quenching Reaction	Reaction Rate Constant (cm^3/s)	Source
Q1	$N_2\,(A^3\Sigma_u^+) + O \rightarrow N_2 + O(^1S)$	1×10^{-11}	Grubbs et al. (2018)
Q2	$N_2\,(A^3\Sigma_u^+) + O \rightarrow N_2 + O$	1.8×10^{-11}	Grubbs et al. (2018)
Q3	$N_2\,(A^3\Sigma_u^+) + O \rightarrow NO + N$	2×10^{-11}	Campbell et al. (2006)
Q4	$N_2\,(A^3\Sigma_u^+) + NO \rightarrow N_2 + NO$	8.9×10^{-11}	Grubbs et al. (2018); Strickland et al. (1999)
Q5	$N_2\,(A^3\Sigma_u^+) + O_2 \rightarrow N_2 + O_2$	4×10^{-12}	Grubbs et al. (2018); Strickland et al. (1999)
Q6	$O(^1S) + O \rightarrow O + O$	2×10^{-14}	Grubbs et al. (2018)
Q7	$O(^1S) + O_2 \rightarrow O + O_2$	$1.6 \times 10^{-12}\chi^{a}$	Grubbs et al. (2018)
Q8	$O(^1S) + O_2 \rightarrow O(^1D) + O_2$	$7.2 \times 10^{-13}\chi^{a}$	Grubbs et al. (2018)
Q9	$O(^1S) + NO \rightarrow O(^1D) + NO$	5.12×10^{-11}	Grubbs et al. (2018)
Q10	$O(^1S) + NO \rightarrow O(^1D) + NO$	2.88×10^{-11}	Grubbs et al. (2018)

Table S1. Quenching Reaction Rate Constants

[a] $\chi = e^{-\left(6750-0.0151T_n^2\right)/8.314T_n}$ where T_n is the neutral temperature in K.

Radiative Transition Reaction	Spectral Feature	Transition Rate (1/s)	Source
$N_2\,(B^3\Pi_g) \rightarrow N_2\,(A^3\Sigma_u^+) + h\nu_{N_2\ 1P}$	N_2 First Positive Bands	2×10^5	Eyler and Pipkin (1983)
$N_2\,(A^3\Sigma_u^+) \rightarrow N_2\left(X^1\Pi_g^+\right) + h\nu_{VK}$	Vegard-Kaplan Bands	0.352	Grubbs et al. (2018)
$O(^1S) \rightarrow O(^1D) + h\nu_{557.7\ \mathrm{nm}}$	O Green Line (557.7 nm)	1.26	Grubbs et al. (2018)

Table S2. Radiative Transition Rates